J. COMBIN. MATH. COMBIN. COMPUT. 127a (2025) 3245--3261

Journal of Combinatorial Mathematics and Combinatorial Computing
www.combinatorialpress.com/jcmcc

Research on point cloud data optimization and feature extraction during 3D reconstruction of high-speed rail wheelsets

Jun Ma[1,✉], Chunguang Zhang[2], Bingzhi Chen[1]

[1] *Institute of Mechanical Engineering, Dalian Jiaotong University, Dalian, Liaoning, 116028, China*

[2] *School of Electrical Engineering, Dalian Jiaotong University, Dalian, Liaoning, 116028, China*

ABSTRACT
With the continuous development of the rail vehicle business, high-speed rail, locomotive, subway, light rail and other railroad transportation industry to reach the prosperity of the previous scene, the wheelset is an important support and walking parts of the rail train, so the detection of its geometric parameters and tread quality of the safe operation of the vehicle is of great significance. In this paper, based on the principle of binocular measurement vision, the mathematical model of bilinear structured light is used to calculate the three-dimensional coordinates of the spatial points of the wheel pairs of high-speed railways. The collected point cloud data are filtered and smoothed to eliminate the noise contained in the data. Integrate the two point data under the same coordinate system, perform data fusion on the overlapping part to complete the alignment of the point cloud. And extract its eigenvalues to realize the point cloud coordinate transformation. Through testing experiments, the accuracy of high-speed rail wheel pair data measurement and other indicators are studied and analyzed. The measurement accuracy of the journal diameter of the HSR wheelset has a deviation of about 0.003 mm compared with the CMM, meanwhile, the fluctuation range of the HSR wheelset diameter data in the left and right directions is within 0.04 mm and 0.03 mm, respectively, and the stability of the measurement data of the model is good. The point cloud rotation error is between -1.09° and 1.09°, and the first quadrant angle error is between -1.114° and 0.829°, and the model controls the error to be around 1°, and the verification of the pairing accuracy is passed, which can meet the requirements of the production and operation activities.

Keywords: bilinear structured light, point cloud data, point cloud alignment, 3D reconstruction, high-speed rail wheelset

✉ Corresponding author.
E-mail address: 1590495168@163.com (J. Ma).
Received 05 March 2024; Revised 15 May 2024; Accepted 20 December 2024; Published Online 15 April 2025.
DOI: 10.61091/jcmcc127a-184

1. Introduction

With the rapid development of China's high-speed railroad, it has gradually become the preferred choice of the public for traveling with its high speed, low noise, comfortable environment, etc. However, the safety requirements during the operation of high-speed railroads have also been improved. Trains are more and more inclined to high-speed and heavy-duty direction development trend, train wheelset to withstand more and more serious thermal stress and centrifugal force and other roles, mainly by the operation of the load force and brake tile, brake caused by the train wheelset near the constant repetition of the applied stress, resulting in stress and fatigue damage and even cracks [1-4]. The two phenomena of train stress concentration and fatigue damage are collectively referred to as early micro-failure, which is an abnormal sign of the early failure of wheelset cracking, which will exacerbate the deterioration of high-speed rail wheelset and wheel-rail system dynamics performance to the extent of manifesting as outwardly intense vibration, noise and other phenomena [5-8]. When the vibration and noise are iterated and repeated to the wheelset, it will accelerate the stress concentration and fatigue damage to the development of macroscopic defects, and rapidly form crack failures. For this kind of situation that produces constant stress concentration and fatigue damage, over time will form cracks in the equipment that can be seen with the naked eye, if not early fault detection, when the macroscopic cracks are found to exist, this situation is very easy to occur a huge catastrophic accidents, at this time, it will not be able to control the fault effectively [9-12]. In order to ensure the safety of train traveling, the relevant railroad departments stipulate that the train wheelsets should be regularly overhauled to inspect the wear degree of the wheelsets as well as to judge whether they are qualified or not, and the key technologies include three-dimensional reconstruction and measurements based on the three-dimensional point cloud [13-16]. Due to the specificity of the geometric location of the wheel and rail contact, the measurement sensor layout is limited, and the current 3D point cloud reconstruction technology can only obtain local point cloud data. Therefore, it is of great practical significance and value to study the optimization of point cloud data and feature extraction in the 3D reconstruction process of high-speed train wheelsets to ensure the safety and reliability of train operation to a greater extent, so that the safety and danger of the passengers and the national investment in the railroad industry can be protected to the greatest extent, and the study of early stress concentration and fatigue damage detection of high-speed train wheelsets is of great practical significance and value [17-20].

In this paper, based on the principle of binocular measurement vision, the three-dimensional spatial points of the rotational translation matrix are derived, and the bilinear structured light measurement system is constructed to obtain the surface point cloud of the measured object. The spatial coordinates in the three-dimensional points are obtained by solving the linear equations of the camera projection matrix associatively. Using the least squares method, the optimal solution of the composed system of super positive definite equations is obtained to get the world coordinates in the spatial 3D points. The collected point cloud data are filtered, smoothed, denoised and cloud-aligned, and the two point cloud data are brought to the same coordinate system, and the point cloud data are optimized by coarse and fine alignment respectively, and the point cloud coordinate transformation is realized after extracting its features, and the specific data of high-speed rail wheel pairs are measured. Through testing experiments, the accuracy and precision indexes of the optimized point cloud data are verified, and the effect of point cloud data smoothing is evaluated.

2. High-speed rail wheelset double line structured light three-dimensional construction

2.1. Camera calibration and 3D reconstruction

2.1.1. Binocular Measurement Vision Principle. Two structural models of binocular measurement systems are known (categorized by the different mounting of the binocular cameras): one in which the two cameras are placed randomly in position. The other is that the two cameras are placed parallel to each other in position, the two imaging planes are coplanar, and the optical axis is perpendicular to the horizontal axis of the camera plane (vertical axis) and perpendicular to the baseline. So there are these two vision systems: (1) horizontally parallel placement of binocular stereo vision system: the baseline is parallel to the horizontal axis of the image plane, (2) vertically parallel placement of binocular stereo vision system: the baseline is parallel to the vertical axis of the camera. In general condition, if the left and right cameras. No special requirements, then the following figure 1 shows the binocular imaging principle diagram.

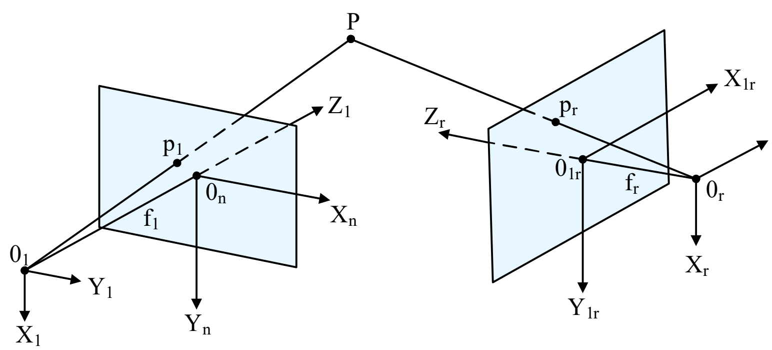

Fig. 1. Binocular schematic

If the left camera is mounted at the origin of the world coordinate system $O_W - X_W Y_W Z_W$ and does not have a rotational behavior (coincides with the world coordinate system), this coordinate system can be noted as $O_1 - X_1 Y_1 Z_1$. This can be obtained by considering $O_{l1} - X_{l1} Y_{l1} Z_{l1}$ as the coordinate system of the image corresponding to the left camera, and f_1 as its focal length, while $O_r - X_r Y_r Z_r$ is considered to be the coordinate system of the right camera, and $O_{lr} - X_{lr} Y_{lr} Z_{lr}$ is considered to be the coordinate system of the outgoing image captured by the right camera, and f_r is the focal length of the right camera:

$$s_1 \begin{bmatrix} X_{l1} \\ Y_{l1} \\ 1 \end{bmatrix} = \begin{bmatrix} f_1 & 0 & 0 \\ 0 & f_1 & 0 \\ 0 & 0 & 1 \end{bmatrix} \begin{bmatrix} X_1 \\ Y_1 \\ Z_1 \end{bmatrix} \tag{1}$$

$$s_r \begin{bmatrix} X_{lr} \\ Y_{lr} \\ 1 \end{bmatrix} = \begin{bmatrix} f_r & 0 & 0 \\ 0 & f_r & 0 \\ 0 & 0 & 1 \end{bmatrix} \begin{bmatrix} X_r \\ Y_r \\ Z_r \end{bmatrix} \tag{2}$$

The mutual position of coordinate systems $O_1 - X_1 Y_1 Z_1$ and $O_r - X_r Y_r Z_r$ can be transformed using the spatial transformation matrix M_{1r}:

$$\begin{bmatrix} X_r \\ Y_r \\ Z_r \end{bmatrix} = M_{1r} \begin{bmatrix} X_1 \\ Y_1 \\ Z_1 \\ 1 \end{bmatrix} = \begin{bmatrix} r_1 & r_2 & r_3 & t_x \\ r_4 & r_5 & r_6 & t_y \\ r_7 & r_8 & r_9 & t_z \end{bmatrix} \begin{bmatrix} X_1 \\ Y_1 \\ Z_1 \\ 1 \end{bmatrix} \tag{3}$$

In Eq. (3), $M_{1r} = \left[R \middle| T \right]$, the rotation matrix $R = \left| r_4 r_5 r_6 \right|$, and the translation matrix $T = \left| t_y \right|$, represent the translation relationship between the origin of both coordinate systems $O_1 - X_1 Y_1 Z_1$ and $O_r - X_r Y_r Z_r$, respectively.

From Eqs. (1)-(3) for spatial points in the $O_W - X_W Y_W Z_W$ coordinate system there exists a correspondence between the two camera image planes:

$$p_r \begin{bmatrix} X_r \\ Y_r \\ 1 \end{bmatrix} = \begin{bmatrix} f_r r_1 & f_r r_2 & f_r r_3 & f_r t_x \\ f_r r_4 & f_r r_5 & f_r r_6 & f_r t_y \\ f_r r_7 & f_r r_8 & f_r r_9 & f_r t_z \end{bmatrix} \begin{bmatrix} Z_1 X_{I1} / f_1 \\ Z_1 X_{I1} / f_1 \\ Z_1 \\ 1 \end{bmatrix} \tag{4}$$

Requested:

$$\begin{cases} X_W = Z_1 X_{n1} / f_1 \\ Y_W = Z_1 X_{n1} / f_1 \\ Z_W = \dfrac{f_1 \left(f_r t_x - X_{tr} t_z \right)}{X_t \left(r_7 X_n + r_8 Y_n + f_1 r_9 \right) - f_r \left(r_1 X_{n1} + r_2 Y_{n1} + f_1 r_3 \right)} \\ \quad = \dfrac{f_1 \left(f_r t_y - X_{tr} t_z \right)}{X_{tr} \left(r_7 X_n + r_8 Y_n + f_1 r_9 \right) - f_r \left(r_4 X_n + r_5 Y_n + f_1 r_6 \right)} \end{cases} \tag{5}$$

From the above equation (5), the coordinates of point $P\left(X_W, Y_W, Z_W \right)$ in three-dimensional space can be found when the parameters f_1 and f_r are known, the two-dimensional coordinates of point $P\left(X_W, Y_W, Z_W \right)$ in the same space corresponding to the coordinate system of the left and right camera images can be computed, and the rotation translation matrix between the two is also known:

$$\begin{cases} s_1 p_1 = M_1 X_W \\ s_r p_r = M_r X_W \end{cases} \tag{6}$$

In the above equation (6), p_1 represents the physical coordinates of the spatial point P in the left camera, p_r represents the physical coordinates of the spatial point P in the right camera, M_1 is the projection matrix of the left camera, M_r is the projection matrix of the right camera, and the 3D spatial point has the following coordinates under the world coordinate system: X_W.

If the left and right cameras are identical and placed parallel in a binocular measurement system, the two imaging planes are coplanar. It can be shown that: $f_1 = f_r = f$, and the derivation process of Eq. (5) can be varied as:

$$\begin{cases} X_W = B \dfrac{X_n}{D} \\ Y_W = B \dfrac{Y_n}{D} \\ Z_W = B \dfrac{f}{D} \end{cases} \tag{7}$$

In the above equation, the distance between the optical centers of the two cameras (baseline distance) is B, and the parallax of the corresponding points in the left and right images is

$D = X_{l1} - X_{tr}$. By this method, the three-dimensional coordinates of the spatial point P in the world coordinate system can be found $\left(X_W, Y_W, Z_W\right)$.

2.1.2. Three-dimensional reconstruction of space points. 3D reconstruction of spatial points of the object under test is an important element in bilinear structured light. One of the common methods to determine the 3D shape of the object under test is to obtain a certain amount of 3D object surface point cloud [21]. When the two cameras are positioned parallel to each other during the shooting process, and M_1 (left camera projection matrix) and M_r (right camera projection matrix) are computed, and the internal references of the left camera and the right camera are the same, while the coordinates of the 3D point coordinates $P\left(X_W, Y_W, Z_W\right)$ are $\left(u_1, v_1\right)$ on the left image pixel coordinate system and $\left(u_r, v_r\right)$ on the right image pixel coordinate system, respectively:

$$\begin{cases} Z_{C1}\begin{bmatrix} u_1 \\ v_1 \\ 1 \end{bmatrix} = \begin{bmatrix} m_{11}^1 & m_{12}^1 & m_{13}^1 & m_{14}^1 \\ m_{21}^1 & m_{22}^1 & m_{23}^1 & m_{24}^1 \\ m_{31}^1 & m_{32}^1 & m_{33}^1 & m_{34}^1 \end{bmatrix}\begin{bmatrix} X_W \\ Y_W \\ Z_W \\ 1 \end{bmatrix} \\ Z_C\begin{bmatrix} u_r \\ v_r \\ 1 \end{bmatrix} = \begin{bmatrix} m_{11}^r & m_{12}^r & m_{13}^r & m_{14}^r \\ m_{21}^r & m_{22}^r & m_{23}^r & m_{24}^r \\ m_{31}^r & m_{32}^r & m_{33}^r & m_{34}^r \end{bmatrix}\begin{bmatrix} X_W \\ Y_W \\ Z_W \\ 1 \end{bmatrix} \end{cases} \tag{8}$$

where $m_{ij}\left(i = 1,2,3; j = 1,2,3,4\right)$ denotes an element in the camera projection matrix M.

$$\begin{bmatrix} \left(u_1 m_{31}^1 - m_{11}^1\right)\left(u_1 m_{32}^1 - m_{12}^1\right)\left(u_1 m_{33}^1 - m_{13}^1\right) \\ \left(u_1 m_{31}^1 - m_{21}^1\right)\left(u_1 m_{32}^1 - m_{22}^1\right)\left(u_1 m_{33}^1 - m_{23}^1\right) \end{bmatrix}\begin{bmatrix} X \\ Y \\ Z \end{bmatrix} = \begin{bmatrix} m_{14}^1 - u_1 m_{34}^1 \\ m_{24}^1 - v_1 m_{34}^1 \end{bmatrix} \tag{9}$$

$$\begin{bmatrix} \left(u_1 m_{31}^r - m_{11}^r\right)\left(u_1 m_{32}^r - m_{12}^r\right)\left(u_1 m_{33}^r - m_{13}^r\right) \\ \left(u_1 m_{31}^r - m_{21}^r\right)\left(u_1 m_{32}^r - m_{22}^r\right)\left(u_1 m_{33}^r - m_{23}^r\right) \end{bmatrix}\begin{bmatrix} X \\ Y \\ Z \end{bmatrix} = \begin{bmatrix} m_{14}^r - u_1 m_{34}^r \\ m_{24}^r - v_1 m_{34}^r \end{bmatrix} \tag{10}$$

By solving the above equation linearly (two planes in three-dimensional space) in conjunction, a straight line (line in space) can be obtained. If the above formula (four planes) joint solution, you can get a point of intersection, the point that is the three-dimensional point of the space coordinates. And the general calculation process, often using the method of least squares, through the optimal solution of the four formulas composed of the system of super positive definite equations, to get the world coordinates of the three-dimensional point P in space.

After the calibration and correction are completed, the left camera differs from the right camera by one baseline distance (in the x-axis direction), assuming that the 3D point P has the following coordinates in the left camera coordinate system: $\left(x_1, y_1, z_1\right)$, and the 3D point P has the following coordinates in the right camera coordinate system: $\left(x_1 - B, y_1, z_1\right)$. From the geometrical relationship of imaging, we can obtain the following equation. The image pixel coordinates of point P in the left and right images are $\left(u_1, v_1\right)$ and $\left(u_r, v_r\right)$. The stereo-corrected longitudinal coordinates of the corresponding points are the same, i.e., $u_1 = v_r$, and there is a difference between the two coordinates:

$$\begin{cases} u_1 - u_0 = f_x \dfrac{x_1}{z_1} \\ v_1 - v_0 = f_y \dfrac{y_1}{z_1} \end{cases} \tag{11}$$

$$\begin{cases} u_r - u_0 = f_x \dfrac{x_1 - B}{z_1} \\ v_1 - v_0 = f_y \dfrac{y_1}{z_1} \end{cases} \tag{12}$$

Associating the above equation, we can get:

$$\begin{cases} X_{C1} = \dfrac{B(u_1 - u_0)}{u_1 - u_r} \\ Y_{C1} = \dfrac{Bf_x(v_1 - v_0)}{f_y(u_1 - u_r)} \\ Z_{C1} = \dfrac{Bf_x}{u_1 - u_r} \end{cases} \tag{13}$$

Where the parallax value is: $u_1 - u_r$, and the baseline of the left camera and the right camera is B, the focal length of the camera in the direction of the u-axis is f_x, and the focal length in the direction of the v-axis is f_y, and the principal point is: (u_0, v_0). It can be seen that, on the basis of obtaining the parallax map as well as the calibration parameters, the three-dimensional coordinates of the spatial point P can be derived by using the coordinates of the pixels of the images of the point P in space on the left camera and the right camera.

After the three-dimensional coordinates of the spatial points are calculated, in some cases, other imageological processes such as denoising, smoothing, etc., need to be performed on them.

2.2. Point cloud data optimization and feature extraction

2.2.1. Point cloud filter denoising. It is inevitable that some noise will be generated in the collected point cloud data, mainly due to three reasons:

1) The interference caused by the surrounding environmental factors, such as the wind around the measurement system, the vibration of nearby objects, the outside world generated by the line of sight interference blocking, and so on.

2) Measurement system reasons, instrument accuracy, the system itself must bring the vibration and so on.

3) In the process of collecting data, the operator's experience, lighting conditions, the surface material and texture characteristics of the measured parts, electromagnetic wave diffraction characteristics, etc. may produce a certain amount of noise. These point cloud noises have a great impact on the subsequent point cloud processing, including alignment data fusion, feature extraction, surface reconstruction and 3D visualization. As soon as the point cloud data is obtained, it needs to be filtered and denoised in the following cases:

(1) Acquired point cloud data with irregular areas of density need to be taken for smoothing [22].

(2) The outlier points collected due to line of sight occlusion, system object boundaries and other issues need to be removed.

(3) The dense point cloud data collected needs to be downsampled.

(4) Noise in the point cloud data needs to be removed. Commonly used filtering methods are mainly the following:

Median filtering eliminates point cloud noise by calculating the statistical median value of each point cloud data point using high frequency signal nonlinearity. This algorithm has a good effect on removing burr point cloud data, but the filtering effect is not ideal for the mixed point class noise that is close to each other. The median filtering algorithm expression is as follows:

$$g(x,y) = med\left\{f(x-k,y-l),(k,l \in W)\right\} \tag{14}$$

where $f(x-k,y-l)$, $(k,l \in W)$ denote the operational data points, and med denotes the median value of all data points monotonically sorted in the window.

Mean value filtering is to homogenize the point cloud point data set, and set the coordinate value of the sampled point as the statistical mean value of each data point of the point cloud in the filtering window, thus replacing the original point. Mean value filtering changes the coordinates of the original data points, which can better smooth the Gaussian noise, but at the same time, it is easy to cause the problem of edge distortion. The expression of the mean value filtering algorithm is as follows:

$$g(x,y) = \frac{1}{mn}\sum_{(r,s)\in S_{mn}}^{n} f(r,s) \tag{15}$$

where S_{mn} is a rectangular filter window of size $m \times n$ centered on (x,y).

Gaussian filtering method with weighted average over the entire point cloud data. Any point and its neighborhood of all point cloud data, and Gaussian function convolution operation, traversing the entire point cloud data, that is, the value of each data point, are weighted average of all data points in its neighborhood to obtain, so as to achieve Gaussian filtering. Because the average effect of Gaussian filtering is small, both to achieve the effect of filtering, but also can be very good to maintain the details of the point cloud data and the original appearance, so it is often used. The specific algorithm of Gaussian filtering is as follows:

Take any point P belongs to the three-dimensional point cloud data, then its neighborhood is expressed as:

$$P_{ij} = \left(X_{ij}, Y_{ij}, Z_{ij}\right)\left|-n \le i \le n, -m \le j \le m\right| \tag{16}$$

Z -coordinate after Gaussian filtering:

$$Z = \frac{1}{c}\sum_{i=-n}^{n}\sum_{j=-m}^{m} Z_{-i-j} G_{ij} \Delta X \Delta Y \tag{17}$$

Where $G_{ij} = \frac{1}{2\pi\sigma^2} e^{-\left(i^2\Delta X^2 + j^2\Delta Y^2\right)/2\sigma^2}$ is the Gaussian function and c is the coefficient.

These three commonly used filtering algorithms for ordered point cloud data can be implemented in MATLAB using the smoothdata function. Date is the point cloud data matrix, method is the filtering processing method, and window is the window length.

2.2.2. Point cloud alignment. Point cloud alignment is performed on the tread surface point cloud data M acquired by the left structured light sensor and the tread surface point cloud data N acquired by the right structured light sensor. The process of point cloud alignment is to integrate the two point cloud data into the same coordinate system, and the overlapping parts are subjected to the process of data fusion. The alignment process is mainly divided into two parts: FPFH coarse alignment and ICP fine alignment [23].

1) Coarse alignment: firstly, use the intrinsic shape signature (ISS) algorithm to find the key points of the treaded point cloud data M and the treaded point cloud data N, the key points here are the

point data that are different and stable relative to the other point sets on the two pieces of point clouds, and the key point extraction steps are as follows:

(1) Search for all points q_j within the radius R neighborhood of each point q_i in the point cloud data and calculate the weights ω_{ij} :

$$\omega_{ij} = 1 / \left\| q_i - q_j \right\|, \left| q_i - q_j \right| < R \tag{18}$$

(2) Calculate the covariance matrix (17) and obtain the matrix eigenvalues, which are $\left\{ \lambda_i^1, \lambda_i^2, \lambda_i^3 \right\}$ in descending order.

$$Cov(q_i) = \sum_{|q_i - q_j| < R} \omega_{ij} \left(q_i - q_j \right) \left(q_i - q_j \right)^T \Big/ \sum_{|q_i - q_j| < R} \omega_{ij} \tag{19}$$

Thresholds γ_1 and γ_2 are set and ISS keypoints are considered to be ISS keypoints if they satisfy $\lambda_i^2 / \lambda_i^1 \le \gamma_1$ and $\lambda_i^3 / \lambda_i^2 \le \gamma_2$. Then FPFH (Point Fast Feature Histogram) algorithm is used to obtain the key point feature descriptors.

PFH (Point Feature Distribution Histogram) feature is to calculate the angular features between a point q_i and all the points in its neighborhood of a certain radius, two by two connected to each other. Take any point q_i and a point q_j and its normals n_i and n_j within the neighborhood, and construct a local coordinate system UVW with q_i as the origin, then the feature relationship between q_i and q_j can be found as follows:

$$\begin{cases} \alpha = V \cdot n_i \\ \varphi = U \cdot \dfrac{q_i - q_j}{d} \\ \theta = \arctan\left(W \cdot n_i, U \cdot n_i \right) \end{cases} \tag{20}$$

where d is the Euclidean distance between two points. Putting $(\alpha, \varphi, \theta, d)$ of all points in the neighborhood into the histogram in a statistical way is the histogram feature of point q_i.

Calculating the SPFH (simplified feature histogram) is to calculate the PFH of the target point and the points in its neighborhood according to the PFH method, while ignoring the relationship between the points in the neighborhood. The final FPFH is obtained as shown below:

$$FPFH(q) = SPFH(q) + \frac{1}{k} \sum_{i=1}^{k} \frac{1}{\omega_k} SPFFH(q_k) \tag{21}$$

where weight ω_k is the distance between q and point q_k in the neighborhood.

The point descriptors of the two point cloud data are compared to find the matching points of the key points of point cloud data M with respect to the key points of point cloud data N, determine the one-to-one correspondence, find the corresponding point covariance matrix and perform the singular value decomposition to obtain R (rotation matrix), T (translation matrix), and to find the centers of mass of the point cloud M and point cloud N:

$$C_m = \frac{1}{K} \sum_{i=1}^{K} m_i, C_n = \frac{1}{K} \sum_{i=1}^{K} n_i \tag{22}$$

where C_m is the center of mass of the point cloud data M, C_n is the center of mass of the point cloud data N, m_i, $n_i \left(i = 1, 2, \ldots, K \right)$ are the coordinates of each point cloud data mass point, and K is the number of point cloud data mass points. Construct the covariance matrix:

$$E_{(3\times3)} = \frac{1}{K} \sum_{i=1}^{K} \left(m_i - C_m \right) \left(n_i - C_n \right)^T \tag{23}$$

Solve $E = U \wedge V^T$ to get $X = UV^T$, that is:

$$R_1 = X, T_1 = C_n - RC_m \tag{24}$$

Based on the matching points of the two point clouds, the transformation matrix tform, $T = \begin{bmatrix} 0.76 & 0 & 0.65 & 0 \\ 0 & 1 & 0 & 0 \\ -0.647 & 0 & 0.76 & 0 \\ 69 & 0 & -34 & 1 \end{bmatrix}$, consisting of rotation matrix R_1 and translation matrix T_1, is obtained to obtain the coarse alignment data of the point cloud.

2) Precision alignment: nearest point iteration (ICP) precision alignment, based on curvature and other features to establish the corresponding point sets P and Q. Assuming two corresponding points p_i and q_j in 3D space, the number of corresponding points in the two point sets is n, and their Euclidean distances are expressed as:

$$d_{(p_i,q_j)} = \sqrt{\left(x_i - x_j\right)^2 + \left(y_i - y_j\right)^2 + \left(z_i - z_j\right)^2} \tag{25}$$

Find the matrices R_2 and T_2 for the variations of P and Q based on the corresponding points, and use least squares to solve the optimal solution so that:

$$e = \sum_{i=1}^{n} \left|\left(Rp_i + T\right) - q_i\right|^2 \tag{26}$$

where e is the error, R_2 is the rotation matrix, and T_2 the translation matrix. Each iteration can find the corresponding R_2, T_2 and error until the number of iterations is reached or the set threshold is satisfied, the final parameters are obtained and the point cloud alignment is completed.

2.2.3. Point cloud coordinate transformation. Align the two pieces of tread point cloud data collected by the two sensors, complete the data fusion, and get the complete tread point cloud data. There is a part of the point cloud data of the tread surface which is the inner surface point cloud data, and it is necessary to extract this part of the point cloud data, firstly, take any point Q_i in the point cloud, and the two neighboring points before and after are Q_{i-1} and Q_{i+1}, and define two vectors from these three points:

$$\begin{aligned} \alpha_1 &= \left(x_{i-1} - x_i\right)i + \left(y_{i-1} - y_i\right)j + \left(z_{i-1} - z_i\right)k \\ \alpha_2 &= \left(x_i - x_{i+1}\right)i + \left(y_i - y_{i+1}\right)j + \left(z_i - z_{i+1}\right)k \end{aligned} \tag{27}$$

Calculate the angle between the two vectors, when the angle is within the preset threshold, it belongs to the medial face point cloud, search in the tread point cloud, extract all the medial face point cloud data, and fit the medial face of the wheel with the overall least squares method, and fit to the spatial plane $AX + BY + CZ = D$. This plane exists at an angle with the XOZ -plane: $\left(\pi/2 - \arctan\left(-A/C\right)\right)$, rotating the overall tread point cloud data by the corresponding angle to bring the inner face parallel to the XOZ -plane.

The plane equation of the inner face of the wheel is obtained as: $2.462 \cdot X + 0 \cdot Y - Z = -352.168$. The overall tread point cloud is rotated by $\left(\pi/2 - \arctan\left(2.462\right)\right)$.

The fused tread point cloud is then transformed from polar to rectangular coordinates to make a circular distribution. The transformation relationship between the Cartesian coordinate system xyz and the cylindrical coordinate system $\rho\varphi z$ is as follows:

$$\begin{cases} x = \rho\cos\varphi \\ y = \rho\sin\varphi \\ z = z + K \end{cases} \tag{28}$$

3. Test experiments and analysis of results

3.1. Data analysis of high-speed rail wheelsets

The optimization of the point cloud data in the frequency domain after its alignment accuracy will affect the calculation of each measurement parameter of the wheelset by the high-speed rail wheelset measurement system. The effect of point cloud data optimization will be analyzed in the following.

3.1.1. Data accuracy. In order to verify the accuracy and stability of the point cloud data optimization and feature extraction in the 3D modeling process of high-speed rail wheelsets proposed in the paper, it was installed at a high-speed rail wheelset production site and carried out a six-month trial, with more than 8 consecutive measurements in each trial. The measurements were carried out in the way of calibration first and then measurement. Limited to space, the article mainly focuses on journal diameter, shoulder distance, medial distance and wheel diameter measurement data, and the rest of the measurement items are similar to the measurement method and measurement principle, so we will not repeat them here.

In order to verify the accuracy of the measured data after increasing the temperature compensation, the data of different wheel pairs measured by the system were manually reviewed. The review test tool is a field real-time calibration measuring instrument, which is calibrated in real time to ensure its accuracy when used as a review instrument. Table 1 shows the accuracy analysis of journal diameter, wheel diameter and medial distance, respectively (the first six groups of data were selected in view of space).

Through the above verification of accuracy, it can be seen that the results of high-speed rail wheelset high-precision measurement system to measure the journal diameter deviation from manual review is less than 0.005 mm, and most of them are between ±0.001~0.002, less than 0.003 mm, the wheel diameter and the length direction dimensions deviation from manual review is less than 0.05 mm, and most of them are between ±0.01~0.02, less than 0.03 mm, so this paper has a good analysis of the accuracy of the wheel diameter, wheel diameter and inside distance. 0.03 mm, so the optimization results of point cloud data in this paper are highly accurate and meet the technical specifications of high-speed rail wheel pair detection.

Table 1. Accuracy analysis

Measurement accuracy of journal diameter						
Wheel	Left journal diameter			Right journal diameter		
	Detection value	Check value	Deviation	Detection value	Check value	Deviation
1	130.453	130.452	-0.001	130.525	130.526	0.001
2	130.454	130.451	-0.003	130.525	130.527	0.002
3	130.453	130.45	-0.003	130.525	130.524	-0.001
4	130.454	130.452	-0.002	130.524	130.524	0
5	130.452	130.452	0	130.523	130.524	0.001
6	130.453	130.452	-0.001	130.525	130.526	0.001
The diameter of the wheel and the accuracy of the measuring size						
Wheel	Left wheel diameter			Right wheel diameter		
	Detection value	Check value	Deviation	Detection value	Check value	Deviation
1	920.655	920.635	-0.02	921.166	921.176	0.01
2	920.657	920.627	-0.03	921.166	921.186	0.02

3	920.655	920.635	-0.02	921.166	921.186	0.02
4	920.655	920.615	-0.04	921.165	921.185	0.02
5	920.656	920.636	-0.02	921.166	921.176	0.01
6	920.655	920.635	-0.02	921.164	921.194	0.03
Wheel	Medial distance			/		
	Detection value	Check value	Deviation			
1	1354.296	1354.306	0.01			
2	1354.296	1354.316	0.02			
3	1354.297	1354.297	0			
4	1354.295	1354.285	-0.01			
5	1354.296	1354.316	0.02			
6	1354.297	1354.307	0.01			

3.1.2. Data reproducibility. During the period from April to August of a certain year, the same pair of wheels is measured at the same position several times and its repeatability is counted to verify the stability of the equipment. Specifically, one or several wheel pairs are selected from the measured wheel pairs or sample wheel pairs and marked at the measurement position, and then repeated measurements are taken at the marked position of the wheel pair in accordance with normal use and to ensure that the measurement position is in the vicinity of the marked position each time. A large number of measurement tests were made at a wheelset production site at different times and under different weather conditions during the period of 5 months before and after the test. For the same CRH3 type high-speed railroad wheelset in April to August monthly measurement data in each randomly selected day's measurement data, the trend is shown in Figure 2. Among them, the left journal and the right journal were measured by CMM at the same time, and the value of their journal diameter (the value is the average of several measurements by CMM, so the figure is a straight line without change) was used as the true value, which was used to compare with the value measured by the equipment to verify the accuracy of the equipment at the same time. The curve in the figure visualizes the accuracy and stability of the measurement results of the measurement system.

The measured temperature range of the above data is 18~28 ℃, the temperature difference between the two calibrations is between ±3 ℃, and the temperature fluctuation range is less than 6 ℃ in the morning and evening working hours. From the above randomly selected data in each month of the past six months, it can be seen that the deviation of journal diameter measurement accuracy compared with CMM is about 0.003 mm, and the fluctuation range of the left journal is within 0.004 mm in most cases, and the fluctuation range of the right journal is within 0.005 mm. The fluctuation range of HRL wheel diameter data in the left and right directions is within 0.04 mm and 0.03 mm, respectively. The stability of the model's measurement data is good from the data level.

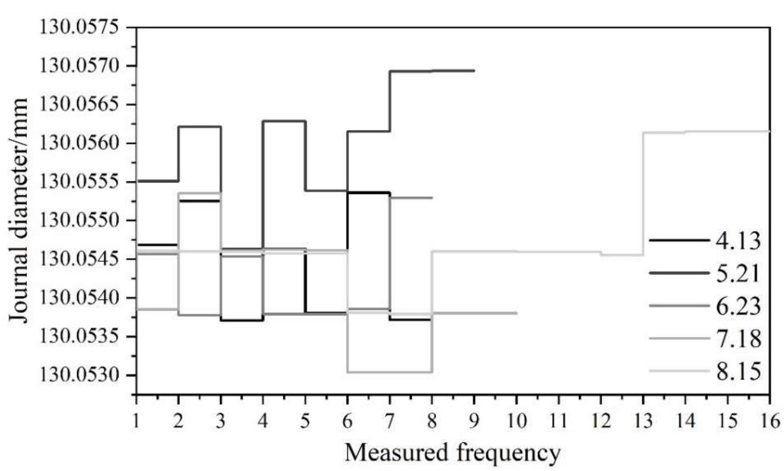

(a)Left journal diameter measurement data

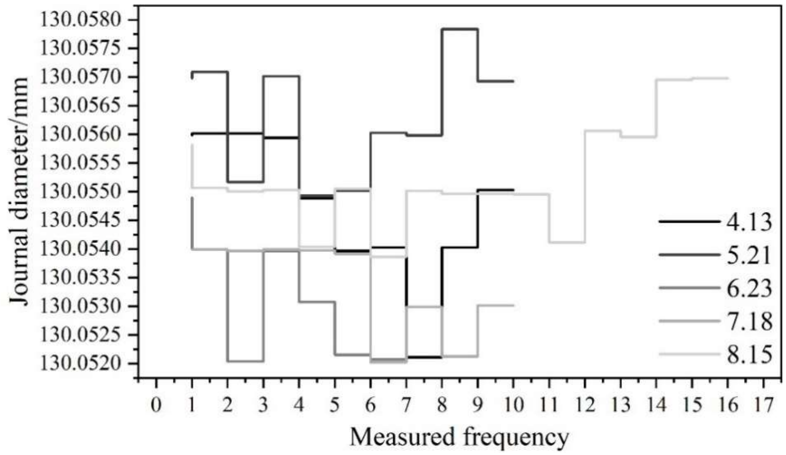

(b)Right journal diameter measurement data

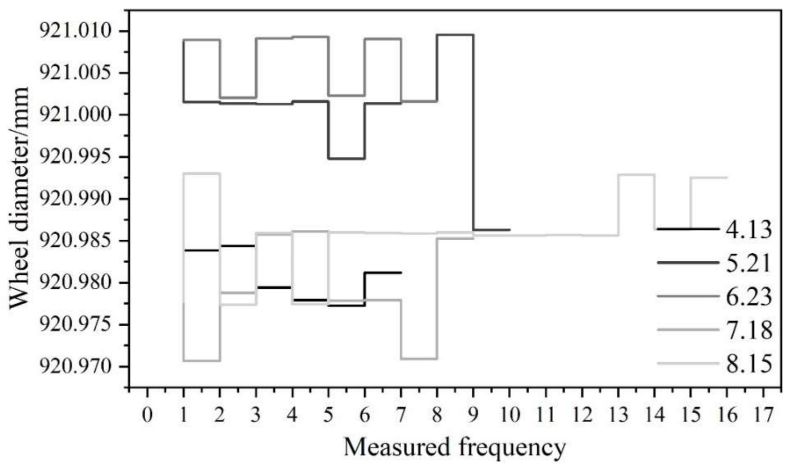

(c)Left-wheel diameter measurement

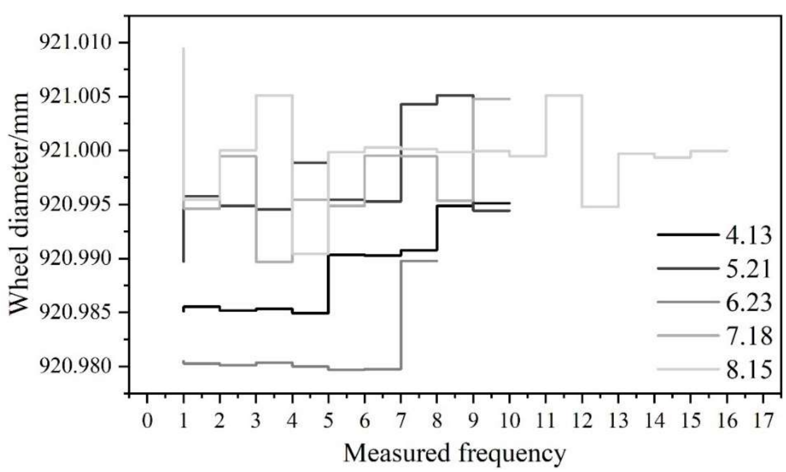

(d)Right wheel diameter measurement

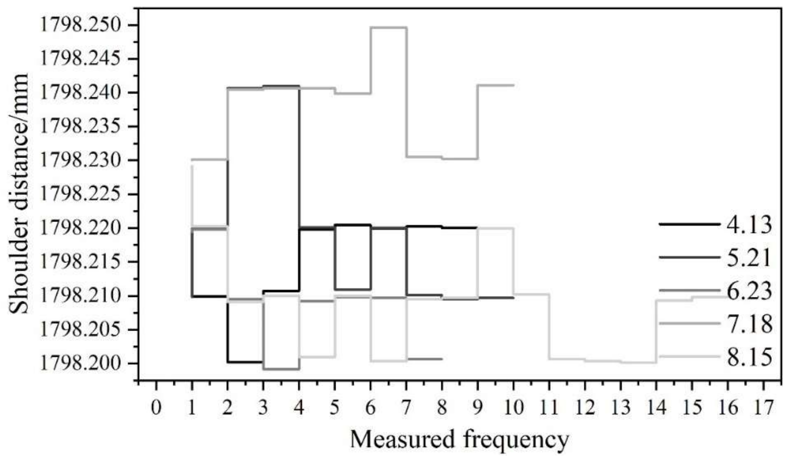

(e)Measurement of shoulder distance

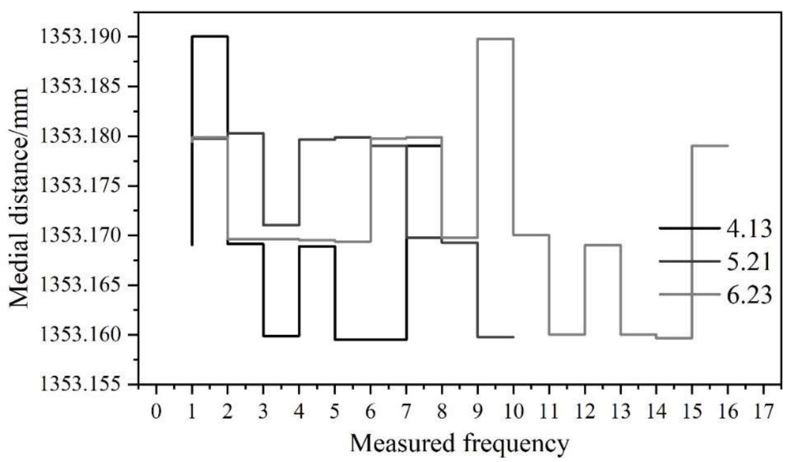

(f)Inner distance measurement

Fig. 2. Measurement of data fluctuations

3.2. Verification of matching accuracy

3.2.1. Translation accuracy. Table 2 shows the comparison results of different translation distance and amplification parameters. According to Table 2, it can be seen that the amplification coefficients corresponding to higher translation accuracy need to be amplified with the same level, and the amplification coefficients corresponding to the detection accuracy of 0.1 mm should be ρ =10. As in the first column of the table, the detection accuracy of 1mm corresponds to a magnification factor of ρ =100, at which time the translation distance in the x and z axes direction is -0.03mm and 0.05mm, respectively, and the calculated translation results are 30 and 50. In summary, it can be concluded that the translation distance does not appear linear or nonlinear error exists with the change of translation distance. At the same time, the influence of the amplification factor on the detection accuracy is determined, and the frequency-domain alignment translation accuracy of the high-speed rail wheel is verified through the optimization of the point cloud data.

Table 2. The comparison results of different translation distances and amplification parameters

Translation distance in x direction (mm)	Z translation Distance (mm)	Amplification factor	Find the phase in the x direction,Pair translation result	Find the translation in the z direction
-0.03	0.05	ρ =100	30	50
-0.3	0.5	ρ =10	3	5

-0.3	0.5	ρ =10	3	5
-0.03	0.05	ρ =100	3	5
-0.05	0.07	ρ =100	0	0

3.2.2. Rotational accuracy. Similarly the selected point cloud is rotated according to the above formula, and for representativeness, rotations are taken at 5° intervals from 0°-360°. And use the coordinate transformation of the point cloud data in section 2.2 to invert the rotation angle.

After a full cycle of 0°-360° calculations, the error values in the first quadrant are cyclically consistent with those in the second, third, and fourth quadrants, and only the first quadrant is shown for convenience. Let the angle of rotation after selecting the point cloud be θ°, the angle obtained be θ, and the difference between the two be $\Delta\theta$. Then, according to the above conditions, the relationship between θ° and $\Delta\theta$ is shown in Fig. 3, from Fig. 3 (a) shows that the initial rotation angle and the inverse angle error is nonlinear, in order to make clear the nonlinear relationship between the two 0-90 ° every 1 ° for the inverse, the inverse error is shown in Fig. 3 (b), Fig. (a)-(b) are the rotation error and the first quadrant angle error, respectively. The rotational error $\Delta\theta$ in Fig. (a) is between -1.09° and 1.09°, and the angular error in the first quadrant is between -1.114° and 0.829°, and the error is controlled to be around 1°.

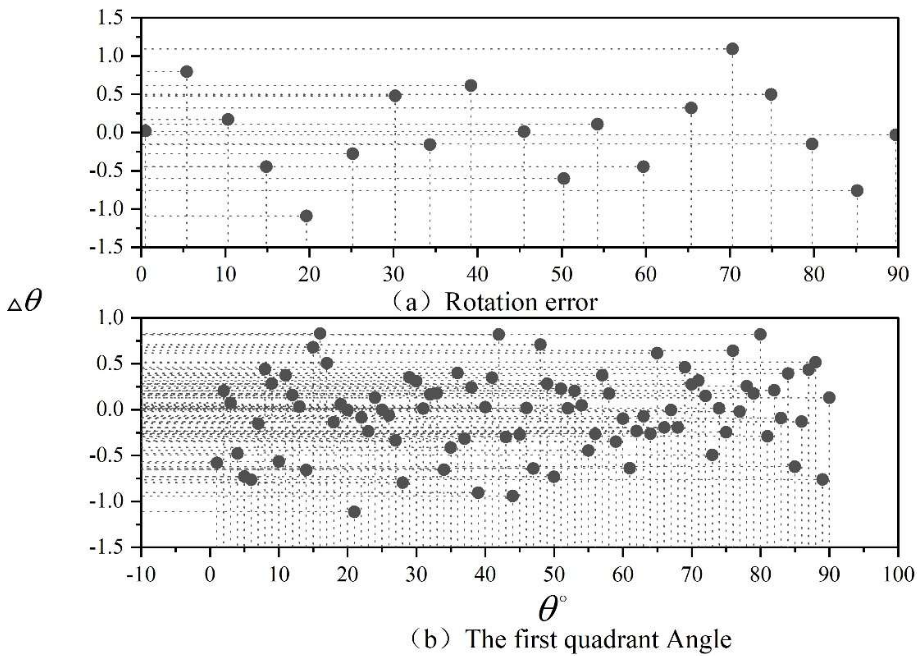

Fig. 3. Rotation accuracy

3.3. *Effect of noise on alignment*

3.3.1. Smoothing effects. As the high-speed rail wheelset is in the process of 3D modeling, the process of light bar centerline extraction introduces digitization errors. The contour data disturbed by environmental factors will form noise. The existence of both errors and noise will affect the calculation of the vertices of the wheel rim and have an impact on the calculation accuracy of the parameters. Therefore, before calculating the measured contour data, the wheelset contour data must be denoised.

Figure 4 shows the comparison of the measured contour before and after smoothing. As can be seen from Figure 4, after the smoothing filter, the noise caused by the environment tends to be concentrated at a few fixed points, before the smoothing of the points are mainly concentrated in the (-25,0), (-30,95), and after the smoothing process, it is concentrated in the two fixed points, respectively (-25,25), (-110, -60) and (0,110), (-60, -10,). The denoising of the contour data is completed by eliminating several classes with small spatial scales.

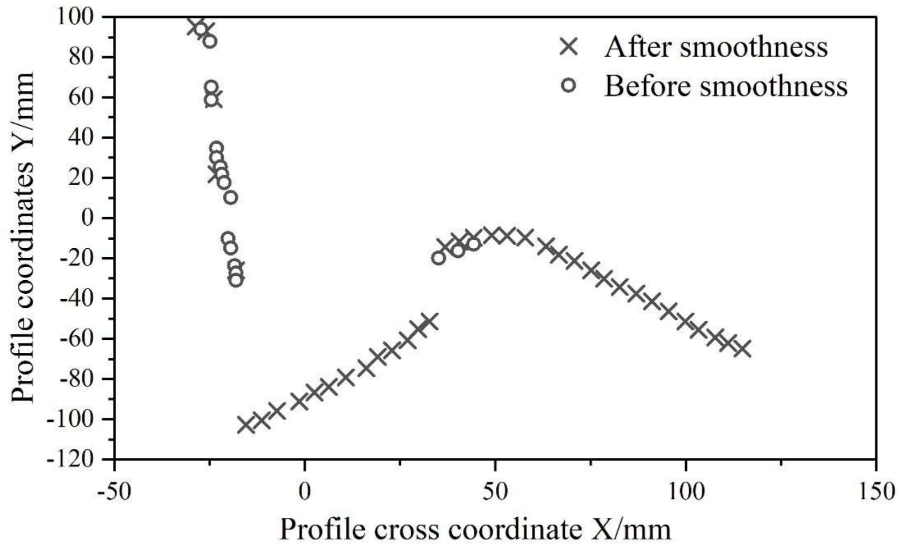

Fig. 4. Contrast the measured contour

3.3.2. Depth value fluctuations. In order to analyze the measurement error of the actual high-speed rail wheelset, the point cloud data obtained from the above experiments are used to analyze the fluctuation in the Z-direction by taking any one point cloud in the X-direction. As shown in Fig. 5.

Calculated from the data in the above figure, the maximum value minus the minimum value is 0.03187 mm, which shows that the fluctuation range of the depth value is small, and the average value is 71.6318.

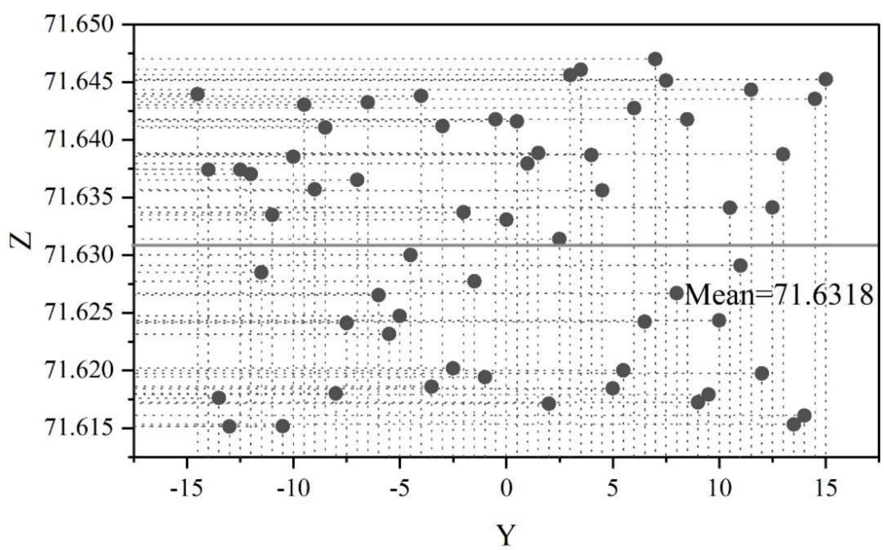

Fig. 5. Depth fluctuation

4. Conclusion

Based on the principle of binocular vision measurement, this paper constructs a mathematical model of bilinear structured light measurement and reconstructs the spatial point 3D model of high speed rail wheelsets in this mathematical model. The point cloud data are filtered and denoised, and the point cloud data are aligned and integrated under the same coordinate axis. Extract the features of one side of the integrated point cloud data surface, and calculate the test values of the aligned HSR wheel pair.

The deviation of the results of the journal diameter of the HSR wheel pairs from the manual review is less than 0.005 mm, most of them are between ±0.001~0.002, and the optimization results of the point cloud data are highly accurate, which meets the requirements of the HSR wheel pair testing.

In the verification of the alignment accuracy of the HSR wheel pair, the translation distance in the direction of x and z axes is -0.03 mm and 0.05 mm, respectively, and the calculated translation results are 30 and 50. The amplification factor will not have any influence on the detection accuracy, so the verification of the frequency domain alignment translation accuracy of the HSR wheel after the optimization of the point cloud data is passed.

After the smoothing filter denoising process of the point cloud data, the noise tends to concentrate at 2 fixed points, which are (-25,25), (-110, -60) and (0,110), (-60, -10), and the influence of noise on the alignment is minimized.

References

[1] Wang, B., Liu, Y., Liao, Y., & Wang, Y. (2024). Analysis of temperature characteristics of high-speed train wheelset system under complex operating conditions. International Journal of Mechanical System Dynamics, 4(3), 331-345.

[2] Zeng, Y., Song, D., Zhang, W., Hu, J., Zhou, B., & Xie, M. (2021). Physics-based data-driven interpretation and prediction of rolling contact fatigue damage on high-speed train wheels. Wear, 484, 203993.

[3] Xiao, Q., Zheng, J., Liu, J., & Fang, J. (2017). Analysis of the wheel/rail rolling contact fatigue of a high-speed train under the transient mechanism. Journal of Mechanical Science and Technology, 31, 2235-2242.

[4] Zhang, Q., Toda-Caraballo, I., Li, Q., Han, J., Han, J., Zhao, J., & Dai, G. (2020). Tension-shear multiaxial fatigue damage behavior of high-speed railway wheel rim steel. International Journal of Fatigue, 133, 105416.

[5] Zhang, G., & Ren, R. (2019). Study on typical failure forms and causes of high-speed railway wheels. Engineering Failure Analysis, 105, 1287-1295.

[6] Cong, T., Han, J., Hong, Y., Domblesky, J. P., & Liu, X. (2019). Shattered rim and shelling of high-speed railway wheels in the very-high-cycle fatigue regime under rolling contact loading. Engineering Failure Analysis, 97, 556-567.

[7] Qu, S., Wang, J., Han, X., & Zeng, J. (2024). Failure analysis on the brake disc hubs with fatigue cracks caused by wheel polygonization. Engineering Failure Analysis, 165, 108781.

[8] Peixoto, D. F., & de Castro, P. M. (2017). Fatigue crack growth of a railway wheel. Engineering failure analysis, 82, 420-434.

[9] Wang, Y. W., Ni, Y. Q., & Wang, X. (2020). Real-time defect detection of high-speed train wheels by using Bayesian forecasting and dynamic model. Mechanical Systems and Signal Processing, 139, 106654.

[10] Bi, Z., Kong, L., & Zhang, J. (2019). Research on Early Fault Detecting for Wheelset of High-Speed Train Based on Metal Magnetic Memory Method. In Recent Developments in Mechatronics and Intelligent Robotics: Proceedings of International Conference on Mechatronics and Intelligent Robotics (ICMIR2018) (pp. 847-856). Springer International Publishing.

[11] Alemi, A., Corman, F., & Lodewijks, G. (2017). Condition monitoring approaches for the detection of railway wheel defects. Proceedings of the Institution of Mechanical Engineers, Part F: Journal of Rail and Rapid Transit, 231(8), 961-981.

[12] Liu, X. Z., Xu, C., & Ni, Y. Q. (2019). Wayside detection of wheel minor defects in high-speed trains by a Bayesian blind source separation method. Sensors, 19(18), 3981.

[13] Jia, X., Yin, Y., & Wang, W. (2024). Dynamic Modeling, Dynamic Characteristics, and Slight Self-Guidance Ability at High Speeds of Independently Rotating Wheelset for Railway Vehicles. Applied Sciences, 14(4), 1548.

[14] Fang, Y., Wang, J., Zhu, Z., Xiao, L., Yuan, T., Liu, X., & Gao, W. (2024). Rapid measurement method for key dimensions of train wheelset based on improved image processing algorithm. Measurement Science and Technology, 35(8), 086012.

[15] Zhang, J., Yao, X., Xing, Z., Cai, C., & Chen, Y. (2024). A Multi-line Structured Light Sensor-Based System for Measuring the Geometries of Train Wheelsets. IEEE Sensors Journal.

[16] Ma, R., Li, J., He, K., Tang, T., Zhang, Y., & Gao, X. (2022). Application of Moire Profilometry in Three-Dimensional Profile Reconstruction of Key Parts in Railway. Sensors, 22(7), 2498.

[17] Qin, C., Wang, Z., Zhang, Y., & Huang, Q. (2017, February). Applications of two phase-height mapping algorithms for PMP in 3D reconstruction of the railway wheel tread. In International Conference on Optical and Photonics Engineering (icOPEN 2016) (Vol. 10250, pp. 464-471). SPIE.

[18] Xie, Y., Cai, W., Li, Y., Yang, J., Liang, S., & Chi, M. (2024). A case study of the economic reprofiling method for a high-speed train's wheel tread in the frequent contact area. Wear, 205244.

[19] Ma, R. Y., Li, J. L., He, K. L., Gao, X. R., Zhang, Y., & Liu, X. Z. (2021, November). Filtering algorithm in 3D reconstruction of wheel tread based on moire profilometry. In Twelfth International Conference on Information Optics and Photonics (Vol. 12057, pp. 228-236). SPIE.

[20] Alemi, A., Corman, F., Pang, Y., & Lodewijks, G. (2019). Reconstruction of an informative railway wheel defect signal from wheel–rail contact signals measured by multiple wayside sensors. Proceedings of the Institution of Mechanical Engineers, Part F: Journal of rail and rapid transit, 233(1), 49-62.

[21] Yikun Luo. (2024). F-PointNet multi-modal 3D object detection based on RGB images and LiDAR point cloud. Advances in Engineering Innovation(1),77-85.

[22] Yang Yi & Fang Hairong. (2021). Research on the Feature Smoothing Algorithm for Point Cloud Data of Large Complex Surfaces Based on Multichannel Convolutional Neural Network. IEEE TRANSACTIONS ON INSTRUMENTATION AND MEASUREMENT.

[23] Fengguang Xiong,Yu Kong,Xinhe Kuang,Mingyue Hu,Zhiqiang Zhang,Chaofan Shen & Xie Han. (2024). A Multi-Scale Covariance Matrix Descriptor and an Accurate Transformation Estimation for Robust Point Cloud Registration. Applied Sciences(20),9375-9375.